The Astrophysical Journal, 751:43 (6pp), 2012 May 20 doi:10.1088/0004-637X/751/1/43

DIRECT MEASUREMENT OF THE ANGULAR POWER SPECTRUM OF COSMIC MICROWAVE BACKGROUND TEMPERATURE ANISOTROPIES IN THE *WMAP* DATA

Lung-Yih Chiang[1] and Fei-Fan Chen[2]
[1] Institute of Astrophysics, National Taiwan University, 1, Rooservolt Road, Taipei, Taiwan; lychiang@asiaa.sinica.edu.tw
[2] Institute of Astronomy and Astrophysics, Academia Sinica, P.O. Box 23-141, Taipei 10617, Taiwan
Received 2011 August 29; accepted 2012 March 8; published 2012 May 3

ABSTRACT

The angular power spectrum of the cosmic microwave background temperature anisotropies is one of the most important characteristics in cosmology that can shed light on the properties of the universe such as its geometry and total density. Using flat sky approximation and Fourier analysis, we estimate the angular power spectrum from an ensemble of the least foreground-contaminated square patches from the *Wilkinson Microwave Anisotropy Probe* *W* and *V* frequency band map. This method circumvents the issue of foreground cleaning and that of breaking orthogonality in spherical harmonic analysis because we are able to mask out the bright Galactic plane region, thereby rendering a direct measurement of the angular power spectrum. We test and confirm the Gaussian statistical characteristic of the selected patches, from which the first and second acoustic peaks of the power spectrum are reproduced, and the third peak is clearly visible, albeit with some noise residual at the tail.

Key words: cosmic background radiation – cosmology: observations – methods: data analysis

Online-only material: color figures

1. INTRODUCTION

The angular power spectrum of the cosmic microwave background (CMB) temperature anisotropies contains a wealth of information about the properties of our universe. The physics behind the shape of the power spectrum at different angular scales is well understood (e.g., see Hu et al.), therefore allowing us to distinguish different cosmological models. The power spectrum possesses specific features, known as acoustic peaks, characterizing compression and rarefaction of the photon-baryon fluid around the decoupling epoch. The NASA *Wilkinson Microwave Anisotropy Probe* (*WMAP*; Bennett et al. 2003a; Spergel et al. 2007; Hinshaw et al. 2009; Jarosik et al. 2011) has produced results that have ushered in the era of "Precision Cosmology," including the angular power spectrum (Hinshaw et al. 2003, 2007; Norta et al. 2009; Larson et al. 2011), from which cosmological parameters are estimated to a high precision (Spergel et al. 2003, 2007; Komatsu et al. 2009, 2011).

However, to retrieve the angular power spectrum, one must separate the foreground contamination from our own galaxy and extragalactic point sources in the observed data (Bennett et al. 2003b; Hinshaw et al. 2007; Gold et al. 2009, 2011). The standard treatment of eliminating galactic diffuse foreground is through multifrequency cleaning, minimum variance optimization for extracting the angular power spectrum, or known foreground templates. Another issue arising from the foreground contamination is the strong emission of the galactic plane for which various masks are adopted by the *WMAP* science team. The masking procedure and incomplete sky coverage thus breaks the orthogonality in the spherical harmonic analysis, which requires additional attention when obtaining the spherical harmonic coefficients (Hivon et al. 2002; Oh et al. 1999; Ansari & Magneville 2010).

Apart from the *WMAP* science team, only a few papers are devoted to the extraction of the CMB power spectrum from raw data (Saha et al. 2006, 2008; Samal et al. 2010; Basak & Delabrouille 2012). They all adopt the methodology of internal linear combination and implement quadratic minimization, which not only minimizes the foreground contamination, but also subtracts the power that is related to the chance correlation between the CMB and foregrounds (Chiang et al. 2009).

In this paper, we present a simple method of direct measurement of the CMB angular power spectrum from *WMAP* raw data, the frequency band maps. By "direct" we mean circumventing any foreground subtraction techniques and avoiding the issue of incomplete sky coverage. We also use *WMAP* frequency band maps, which are made possible for power spectrum extraction after the Chiang & Chen (2011) estimate of the corresponding window functions.

This paper is arranged as follows. In Section 2, we review the flat sky approximation and then we discuss the issue of foregrounds, instrument noise, and window function in Section 3. We test the Gaussianity of the patches taken from *WMAP* data in Section 4. We then employ the method in Section 5, and we discuss the results in Section 6.

2. FLAT SKY APPROXIMATION

Standard treatment for whole-sky CMB spectral analysis involves writing the temperature anisotropies as a sum of spherical harmonics $Y_{\ell m}$: $T(\theta,\varphi) = \sum_\ell \sum_m a_{\ell m} Y_{\ell m}(\theta,\varphi)$, where θ and φ are the polar and azimuthal angles, respectively, $a_{\ell m} \equiv |a_{\ell m}| \exp(i\phi_{\ell m})$ is the spherical harmonic coefficient, and $\phi_{\ell m}$ is the phase. The strict definition of an isotropic Gaussian random field (GRF) requires that the real and imaginary parts of the $a_{\ell m}$ are mutually independent and both are Gaussian; however, a more convenient definition is that the phases are uniformly random on the interval $[0, 2\pi]$. The power spectrum can be estimated as $C_\ell = (2\ell+1)^{-1} \sum_m |a_{\ell m}|^2$.

However, to estimate the power spectrum from small square patches, one can use the fast Fourier transform (FFT):

$$T(\boldsymbol{r}) = \sum_{\boldsymbol{k}} a_{\boldsymbol{k}} \exp\left[\frac{2\pi i(\boldsymbol{r}\cdot\boldsymbol{k})}{N}\right], \tag{1}$$

where $\boldsymbol{r} \equiv (\theta,\varphi)$ and $\boldsymbol{k} \equiv (k_\theta, k_\varphi)$ if the patches are chosen on the equator with the sides aligned with the spherical coordinates.

The power spectrum from the patch is $C_k \equiv \langle |a_{\boldsymbol{k}}|^2 \rangle$, where the angle brackets denote the average for integer k over all $|a_{\boldsymbol{k}}|^2$ for $k - 1/2 \leqslant |\boldsymbol{k}| < k + 1/2$. The scaling relation between Fourier wavenumber k and multipole number ℓ is $\ell = 2\pi k/L$, where L is the patch size. The angular power spectrum C_ℓ at multipole number ℓ is scaled from C_k at Fourier wavenumber k via

$$C_{\ell=2\pi k/L} = L^2 C_k. \tag{2}$$

If the signal is white noise, the scaling relation can be easily understood as follows. For spherical harmonic analysis, $C_\ell = 4\pi\sigma^2_{\rm sky}/N_{\rm sky}$, whereas, for FFT on a patch taken from the sky, $\sigma^2_{\rm patch} = C_k N_{\rm patch}$, where $N_{\rm sky}$ is the total pixel number of the sphere and $N_{\rm patch}$ is the pixel number of the patch. Since white noise is homogeneous, $\sigma^2_{\rm patch} = \sigma^2_{\rm sky}$, then $C_\ell = 4\pi C_k N_{\rm patch}/N_{\rm sky} = C_k L^2$. Note that the scaling relation can be applied with minimum error for patches centered at $\theta = \pi/2$ if one uses a nonequal area pixelization scheme.

According to the scaling relation, the largest scale (smallest ℓ) at which one can obtain the power is $\ell_{\rm min} = 2\pi/L$,[3] then the multiple numbers are sampled with the interval $\Delta\ell = 2\pi/L$ down to the smallest scale, which is decided by the size of the pixel p: $\ell_{\rm max} = \pi/p$. So, the disadvantage of estimating the power spectrum from patches is that the sampling interval $\Delta\ell$ is much larger than one, which can be viewed as intrinsic binning.

In Figure 1 we test the scaling relation of Equation (2). We simulate a full-sky CMB map with *WMAP* best-fit ΛCDM model and take 100 patches, each $24^\circ \times 24^\circ$ with a pixel size of 3 arcmin. One can see that the mean power spectrum from the 100 patches fits nicely with the input power spectrum, and the error from the discontinuous boundary condition usually present in data analysis of square patches is negligible at the interested scales. In the bottom panel we show the difference between the mean and input spectrums. Although the error varies due to different realizations for low multipoles, the trend is such that the error from the flat sky approximation mainly appears at peaks and troughs where the peaks are not high enough and the troughs are not low enough, which is around 100 μK^2.

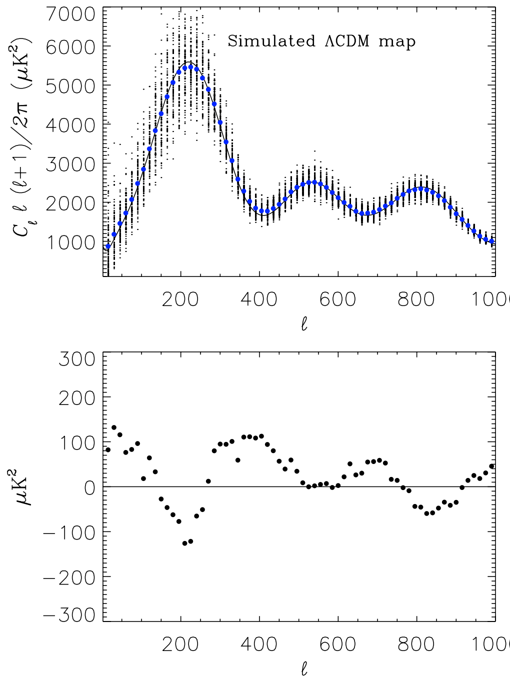

Figure 1. Test of the scaling relation of Equation (2) in the flat sky approximation. We simulate a full-sky CMB map with *WMAP* best-fit ΛCDM model and take 50 patches of a $24^\circ \times 24^\circ$ square with a pixel size of 3 arcmin. The power spectra of the patches are scaled with a factor $(2\pi/15)^2$ and the sampling interval of the multipole numbers $\Delta\ell = 15$. The scaling relation is shown in the top panel. The dots are from 100 patches and the mean is denoted by big blue dots. The mean power spectrum, after scaling according to Equation (2), fits nicely with the input one. In the bottom panel, we show the difference between the mean and the input spectrum, and one can see the error mainly comes from peaks and troughs.

(A color version of this figure is available in the online journal.)

3. DIRECTLY RETRIEVING THE CMB POWER SPECTRUM

The signal T_ν in the sky at frequency ν is a combination of the CMB signal $T_{\rm c}$ and diffuse foregrounds (synchrotron, free–free, and dust emission) plus extragalactic point sources, altogether denoted as total foreground F_ν. They are measured with an antenna beam B_ν:

$$T_\nu = (T_{\rm c} + F_\nu) \otimes B_\nu + N_\nu, \tag{3}$$

where $\otimes$ denotes convolution and N_ν is the instrument noise. To reach the CMB power spectrum, we discuss below the three parts of Equation (3): foreground contamination, noise, and the window function.

3.1. Foreground Contamination and Dispersion Threshold

The NASA Cosmic Background Explorer has measured the CMB temperature fluctuation at a level 10^{-5} with 10° FWHM (Smoot et al. 1992). From Equation (3), the variance of the measured T_ν includes the foreground component:

$$\sigma^2_\nu = \sigma^2_{\rm c} + \sigma^2_{F_\nu} + \sigma^2_n + {\rm Cov}\left[T^{\rm sm}_{\rm c}, F^{\rm sm}_\nu\right] + {\rm Cov}\left[T^{\rm sm}_{\rm c}, N_\nu\right] + {\rm Cov}\left[F^{\rm sm}_\nu, N_\nu\right], \tag{4}$$

where $\sigma^2_{\rm c}$, $\sigma^2_{F_\nu}$, and σ^2_n are the variance of the beam-convolved CMB, beam-convolved foreground, and noise at frequency ν, respectively, and the last three terms denote their covariances. For an ensemble of small patches, the average

$$\left\langle\sigma^2_\nu\right\rangle = \left\langle\sigma^2_{\rm c}\right\rangle + \left\langle\sigma^2_n\right\rangle + \left\langle\sigma^2_{F_\nu}\right\rangle \geqslant \left\langle\sigma^2_{\rm c}\right\rangle + \left\langle\sigma^2_n\right\rangle. \tag{5}$$

The CMB fluctuations (and noise) always persist in each patch, but those from the foreground do not. Thus, we can choose patches with lower variances because they contain less foreground contamination, thereby providing a better estimation of the CMB power spectrum. Therefore, one can use the dispersion threshold $\sigma^{\rm th}$ for controlling the foreground contamination level among the patches.

The power spectrum is a spread of the variance into different scales, so, from Equation (5), $\langle C^\nu_k\rangle = (\langle C^{\rm c}_k\rangle + \langle f^\nu_k\rangle)\mathcal{W}^\nu_k + \langle n^\nu_k\rangle$, where $C^{\rm c}_k$ is the power spectrum of the CMB, $\mathcal{W}^\nu_k$ is the window function, and C^ν_k, f^ν_k, and n^ν_k are the power spectrum of the band signal, total foreground, and instrument noise of frequency ν at wavenumber $k = \ell L/2\pi$, respectively. For the *WMAP* V and W band where the CMB dominates over the foreground outside the galactic plane, patches with variances below a threshold

[3] Usually, one associates multipole number ℓ with a characteristic angular scale ϖ on the sphere via $\ell = \pi/\varpi$ because a characteristic angular scale (e.g., a scale between a cold and a hot spot) is one-half of one full wavelength, i.e., $\varpi = L/2$.

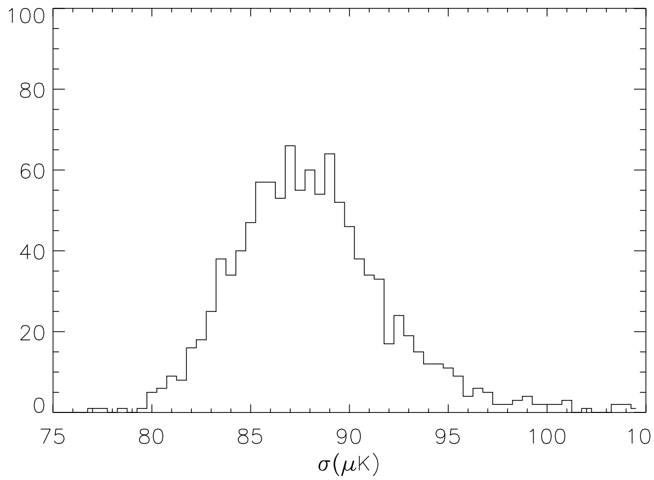

Figure 2. Histogram of the CMB fluctuation from 1000 $24° \times 24°$ patches taken from simulated full-sky maps with a FWHM beam of 19 arcmin. The mean is at 88.34 μK.

$\sigma_v^2 < \sigma_{\mathrm{th}}^2$ shall give

$$\langle C_k^v \rangle \simeq \langle C_k^c \rangle \mathcal{W}_k^v + \langle n_k^v \rangle. \tag{6}$$

We simulate *WMAP* *V* band (i.e., with a FWHM beam of 21 arcmin) full-sky CMB maps and take, in total, 1000 patches of a $24° \times 24°$ square and plot the histogram of the dispersion σ in Figure 2. The mean lies at 88.34 μK, which provides an indication of our choice of the dispersion threshold.

There is a concern that, by using variance as the criterion, we select patches not only with less foreground contamination, but also with covariances that are negative to reduce the variance, thus creating bias. Of all the patches, the distributions of the variances of the first three terms in Equation (4) have a positive mean and spread, whereas those of the covariance terms are distributed around zero due to the Gaussianity of both the CMB and the noise. To see this, we take *WMAP*-derived *V*-band foreground (smoothed to 1°from the maximum entropy method (MEM), *WMAP* simulated noise in the *V* band,[4] and simulate ΛCDM CMB; also smoothed to 1°). In the top panels of Figure 3, we plot the histograms of the patches for the six terms in Equation (4). We then add them together to simulate the observed signal and plot the histograms of the six components of the patches with threshold $\sigma < 0.12$. One can see that patches with a larger-variance foreground component are excluded in the process. More importantly, the negative tail of the covariance term between the CMB and foreground is also eliminated. The reason for this is that for a single patch the variance of the foreground component is not independent of the covariance foreground and CMB or of the covariance between the foreground and noise, and both tails in the histogram of the covariance between the CMB and foreground (orange) are from highly non-Gaussian foreground components, which will manifest themselves in high variances. Thus, when we exclude patches with the higher-variance foreground, we simultaneously eliminate negative covariances. The same argument applies to tails of the covariance between the foreground and noise.

Another concern is that by choosing low-variance patches we are choosing a CMB quiet area that might result in a lower power spectrum. In Figure 4, we demonstrate that unless a significantly low threshold is chosen (which would result in few patches), using a low variance as a criterion still provides a fair sample for estimating the power spectrum.

3.2. Cross-power Spectrum to Eliminate Noise

To eliminate the noise after choosing patches with low variance, we can employ the cross-power spectrum (XPS) on the same patch of sky at different frequency bands. XPS is a quadratic estimator between two maps (or patches) a and b, whose Fourier modes are $a_{\boldsymbol{k}}$ and $b_{\boldsymbol{k}}$:

$$x_k^{ab} = \frac{1}{2}\big\langle \big(a_{\boldsymbol{k}}^* b_{\boldsymbol{k}} + b_{\boldsymbol{k}}^* a_{\boldsymbol{k}}\big)\big\rangle, \tag{7}$$

where $*$ denotes a complex conjugate and the angle brackets have the same notation as in Equation (2). The advantage of XPS as an unbiased quadratic estimator for the power spectrum estimation lies in the fact that XPS returns with its usual power spectrum $\langle |a_{\boldsymbol{k}}|^2 \rangle$ if a and b are of the same signal. If a and b are uncorrelated, then XPS reduces the signal by (Chiang & Chen 2011)

$$\frac{\sqrt{\big\langle \big({X_k}^{ab}\big)^2 \big\rangle}}{\sqrt{A_k B_k}} \simeq \frac{1}{\sqrt{2\pi k}}, \tag{8}$$

where A_k and B_k are the power spectrum of signals a and b, respectively. The decreasing of the uncorrelated signal is inversely proportional to the square root of the number of the random walk, and it can be further decreased by $1/\sqrt{LN}$ with binning $L \equiv \Delta\ell$ multipole numbers and averaging from N sets of XPS. Therefore, XPS is useful in reducing uncorrelated signals while preserving the correlated one, which is employed by *WMAP* to extract the CMB spectrum by crossing the foreground-cleaned maps from differencing assemblies (DA; Hinshaw et al. 2003, 2007; Norta et al. 2009; Larson et al. 2011).

For patches on the *V* and *W* band map with low variances, hence a satisfied Equation (6), we can write $a_{\boldsymbol{k}}^V = a_{\boldsymbol{k}}^c b_{\boldsymbol{k}}^v + n_{\boldsymbol{k}}^v$ and $a_{\boldsymbol{k}}^W = a_{\boldsymbol{k}}^c b_{\boldsymbol{k}}^w + n_{\boldsymbol{k}}^w$, where $a_{\boldsymbol{k}}^c$ is the Fourier mode of CMB, $b_{\boldsymbol{k}}^v$ and $b_{\boldsymbol{k}}^w$ are that of the *V* and *W* band beam, and $n_{\boldsymbol{k}}^v$ and $n_{\boldsymbol{k}}^w$ are that of the *V* and *W* band noise, respectively. In XPS, the correlated signal $\langle |a_{\boldsymbol{k}}^c|^2 b_{\boldsymbol{k}}^v b_{\boldsymbol{k}}^w \rangle$ is what we look for, whereas those uncorrelated terms between CMB and noises ${X_k}^{\mathrm{cw}}$, ${X_k}^{\mathrm{cv}}$ and between noises ${X_k}^{vw}$ will be decreased according to Equation (8).

3.3. Window Functions of the Frequency Band Maps

The window functions of the *WMAP* DA maps are directly measured from Jupiter (Page et al. 2003; Hill et al. 2009) and are available at the official Web site.[5] The frequency band maps, however, are combined from the DA maps, so the corresponding window functions do not exist. Note that the window functions of the DA maps have different profiles even at the same frequency band, particularly for the *W* frequency band. It is then demonstrated in Chiang & Chen (2011) that the window functions of the frequency band maps can be estimated from bright point sources, and they show that the window function of the *W* band map takes the form of W1 DA, whereas the *V* band takes the form of V1 or V2 DA.

[4] Both are taken from http://lambda.gsfc.nasa.gov/product/map/current/.

[5] http://lambda.gsfc.nasa.gov/product/map/current/

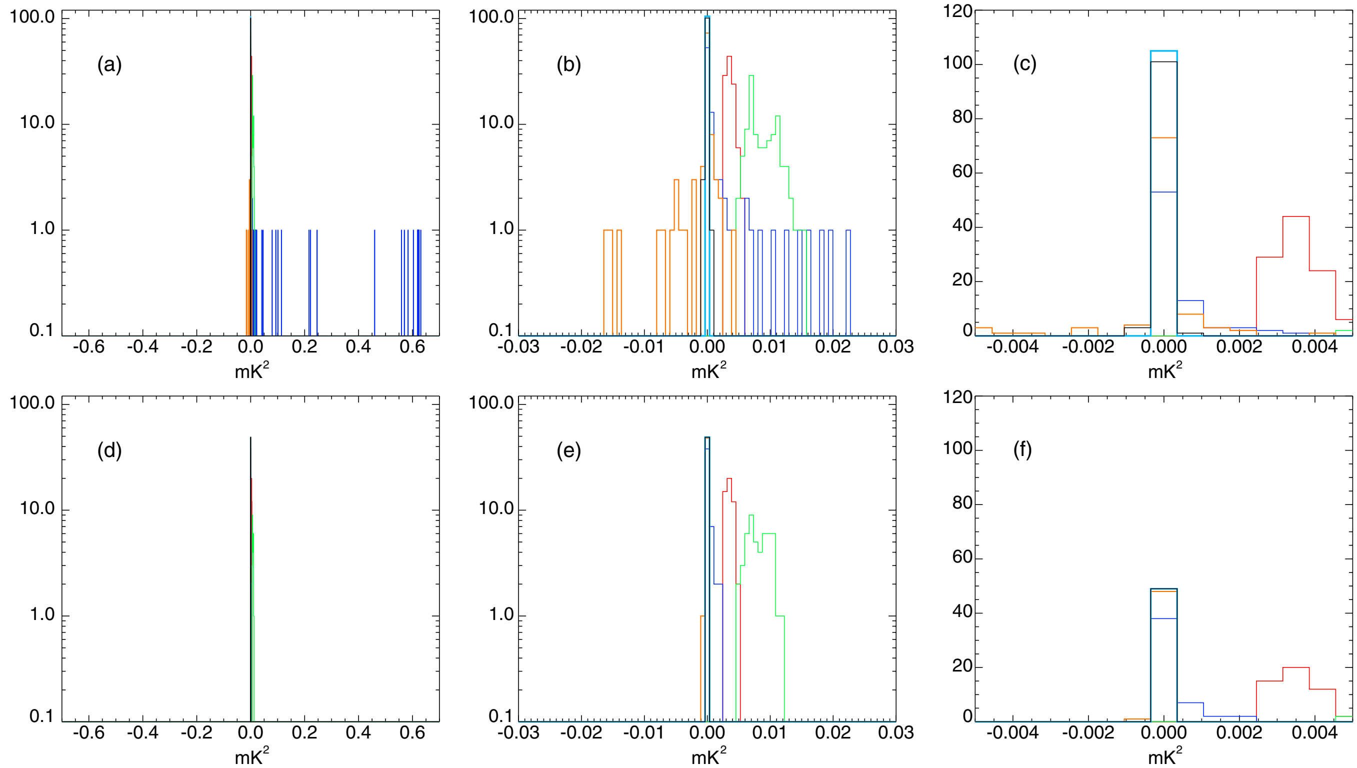

Figure 3. Demonstration of foreground elimination by choosing low-variance patches. We simulate the measured signal with the best-fit ΛCDM CMB, MEM-extracted foreground, and simulated noise in the V band. The histograms of the six terms from Equation (4) are plotted in the top panels: variance of the CMB (red), foreground (blue), noise (green), covariance between the CMB and foreground (orange), between the CMB and noise (light blue), and between the foreground and noise (black), where (b) and (c) are blown-up graphs of (a). After setting criterion $\sigma = 0.12$, we plot the histograms of the 49 selected patches in the bottom panels, where (e) and (f) are blown-up graphs of (d). In selecting the low-variance patches, we exclude the high-variance, non-Gaussian foreground (comparing the blue curve in (a) and (d)) and the two tails of the covariance between the foreground and CMB (comparing the orange curve in (b) and (e), and in (c) and (f)).

(A color version of this figure is available in the online journal.)

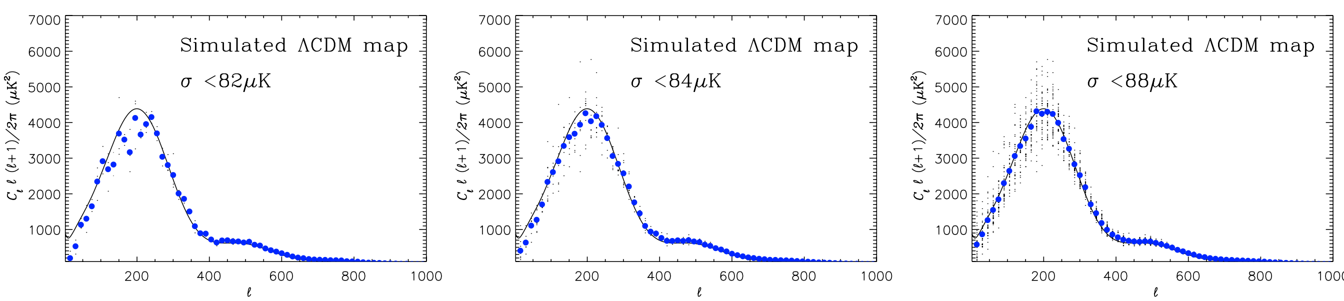

Figure 4. Demonstration of CMB quiet areas from a low variance. From a simulated V band CMB map (high ℓ are smoothed by a FWHM beam of 21 arcmin), we set a different threshold $\sigma^{\rm th}$ to see if choosing CMB quiet areas affects the estimation of the power spectrum. In the left panel, we choose a threshold $\sigma^{\rm th} = 82\,\mu$K with only three patches in the plot. The mean power spectrum (big blue dot) is indeed lower than the input one (solid line), particularly for low ℓ. In the middle panel, we plot the nine patches that have σ lower than 84 μK. On the right panel with $\sigma^{\rm th} = 88\,\mu$K (the mean from Figure 2), one can see that the mean power spectrum from 34 patches fits well with the input one.

(A color version of this figure is available in the online journal.)

4. GAUSSIANITY OF THE PATCHES

The simplest inflation theory predicts the CMB anisotropies, amplified from quantum fluctuations, and constitute a GRF (Bardeen et al. 1986; Bond & Efstathiou 1987). If the CMB is indeed statistically isotropic Gaussian, the angular power spectrum furnishes a complete statistical description. One way to test Gaussianity is through phases. The central limit theorem guarantees that a superposition of a large number of harmonic modes will be close to Gaussian as long as the phases from harmonic analysis are uniformly random in $[0, 2\pi]$. Based on the random phase hypothesis, we can test Gaussianity of the selected patches by employing the Shannon entropy of Fourier phases $\mathcal{S} = -\sum p_i \ln p_i \delta\phi$, where $p_i \delta\phi$ is the distribution probability at the ith interval in $[0, 2\pi]$ and $\sum p_i \delta\phi = 1$. It can be used to test for uniformity: $p \equiv p(\phi_k)$ and independence (nonassociation): $p \equiv p(D)$ where $D(\Delta k) = \phi_{k+\Delta k} - \phi_k$ (Chiang & Coles 2000; Coles & Chiang 2000). If the phases are uniformly random, then $p_i = (2\pi)^{-1}$ and the entropy reaches a maximum $\mathcal{S}_{\rm max} = \ln 2\pi$. In Figure 5, we plot the histogram of the Shannon entropy for phase difference $\Delta k = 1$ and 2. We also plot 1000 Gaussian patches to test significance. If we set

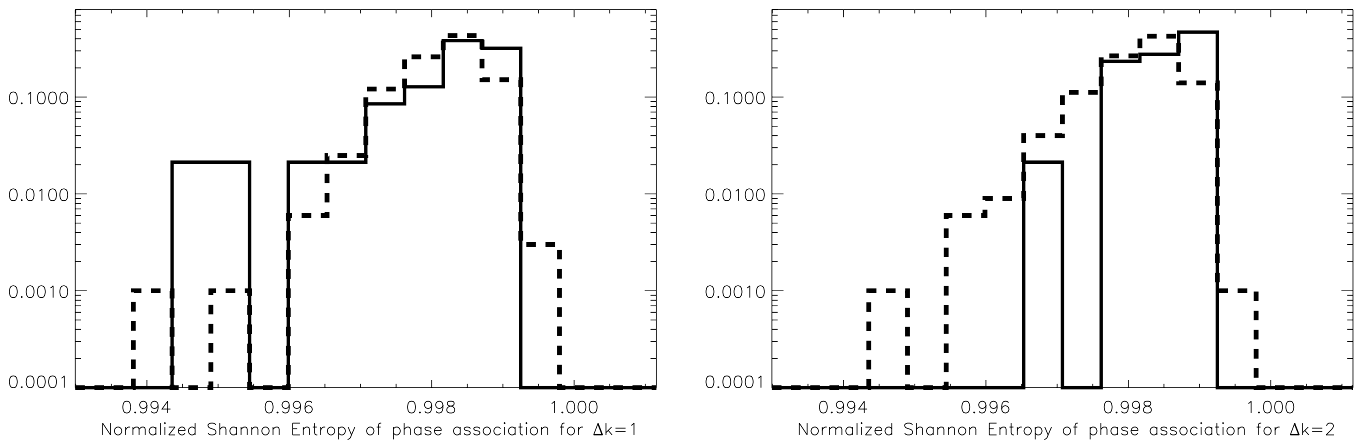

Figure 5. Normalized histogram of the Shannon entropy for Fourier phase association from the 47 selected patches. The phases of the Fourier modes that are equivalent to multipole number $\ell \leqslant 1050$ are taken for calculation. The Shannon entropy $\mathcal{S}$ of the phase association between $\Delta k = 1$ is shown on the left panel and $\Delta k = 2$ is shown on the right. The normalized histogram for the 47 patches is shown in solid curves. For comparison, we plot in the dashed curve the histogram from 1000 $24^\circ \times 24^\circ$ patches taken from full-sky Gaussian maps. With a significance level at 0.001, none of the 47 patches are rejected by the Gaussian hypothesis via the Shannon entropy.

the significance level at 0.001, then none of the 47 patches are rejected by the Gaussian hypothesis.

5. ANGULAR POWER SPECTRUM OF THE CMB FROM THE *WMAP* FREQUENCY BAND MAPS

In this section, we apply our method on *WMAP* frequency *V* and *W* band maps to extract the CMB angular power spectrum via Fourier analysis on the $24^\circ \times 24^\circ$ patches. Although one can take patches with a smaller size and render more patches from the entire sky, this would increase the noise power spectrum level and, consequently, the XPS residual shown in Equation (6).

We first take the *WMAP V* band and choose 47 patches with $\sigma < 98\mu$K (after deleting the bright point sources exceeding 5σ of the patch). Note that in Figure 2 the mean of the 1000 patches is $\sigma = 88.34\,\mu$K, but those taken in real maps with pixel noise have higher values. Before extracting the power spectrum, we test the Gaussianity of the 47 patches by employing the Shannon entropy of Fourier phases for their association. In Figure 5, we show the normalized histogram of the Shannon entropy for the associated phases for $\Delta k = 1$ on the left and 2 on the right. We also plot the histogram from 1000 $24^\circ \times 24^\circ$ Gaussian patches.

We then calculate the XPS from the same patches of the *V* and *W* band to eliminate the noise. They are then deconvolved by $(\sqrt{W_V W_W})^{-1}$, where W_V and W_W are the window function of the *V* and *W* frequency band map, respectively. The retrieved angular power spectrum is shown in Figure 6. One can see that our simple method yields the CMB power spectrum with a clear first and second Doppler peak, which matches the result from the *WMAP* science team. The third peak is also visible, albeit with a higher amplitude at the tail than theirs, which is due to the residual from XPS. In the bottom panel, we plot the difference of our mean power spectrum and the binned one from the *WMAP* science team. In addition, we the result from our method with the *WMAP* power spectrum, and we correct the difference with the systematic error from the flat sky approximation shown in the bottom panel of Figure 1. One can see that the difference at multipole range $\ell \sim 150$–500 is reduced.

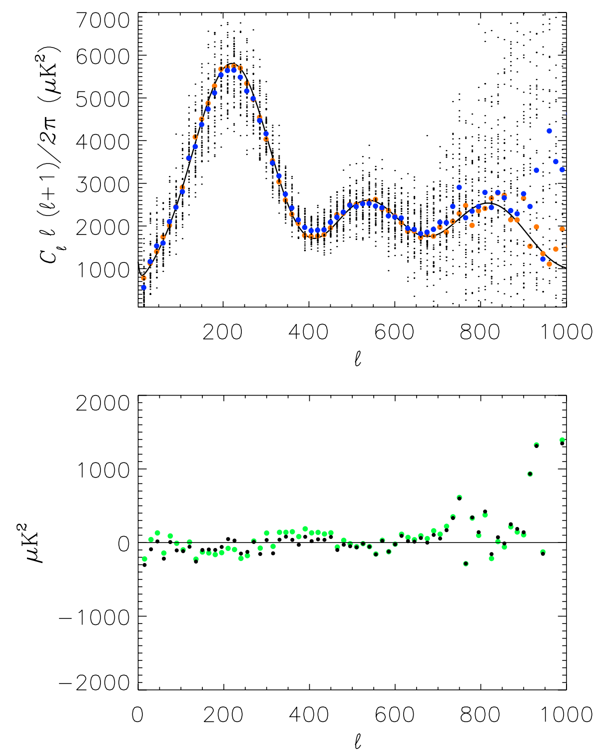

Figure 6. Direct measurement of the CMB angular power spectrum. From *WMAP V* band map, we choose patches with $\sigma < 98\,\mu$K (after eliminating bright point sources), and we take the cross-power spectra of the patches between *WMAP V* and *W* band. Top panel: after deconvolution of the window functions, the power spectra of the 47 patches are shown in the black dot and the mean power spectrum in the big blue dot. For comparison, we plot the power spectrum binned ($\Delta\ell = 15$) (big orange dot) from that of the *WMAP* science team. The best-fit ΛCDM model is in the solid line. *Bottom panel:* we show the difference of our the mean power spectrum and the binned one from the *WMAP* science team (green dot). To compare the result from our method with the *WMAP* power spectrum, we correct the difference with the systematic error from the flat sky approximation shown in the bottom panel of Figure 1 (black dot).

(A color version of this figure is available in the online journal.)

6. DISCUSSION

Since the release of the *WMAP* data, full-sky analysis has become the standard method for estimating the power spectrum because it has offered for the first time a detailed measurement at super-horizon scales. The method we present in this paper utilizes small patches, so it has an intrinsic limitation on the largest scale we can measure. Nevertheless, it adopts a completely different methodology and provides a more intuitive way to obtain the power spectrum on all but the very largest of scales.

We acknowledge the use of the HEALPIX[6] package (Górski et al. 2005) and the use of the GLESP[7] package (Doroshkevich et al. 2005). The author thanks Peter Coles, Andrew Jaffe, Dipak Munshi, and Keiichi Umetsu for useful discussions and suggestions. This work is supported by the National Science Council Grant NSC 98–2112–M–001–001–MY3.

REFERENCES

Ansari, R., & Magneville, C. 2010, MNRAS, 405, 1421
Bardeen, J. M., Bond, J. R., Kaiser, N., & Szalay, A. S. 1986, ApJ, 304, 15
Basak, S., & Delabrouille, J. 2012, MNRAS, 419, 1163
Bennett, C. L., Halpern, M., Hinshaw, G., et al. 2003a, ApJS, 148, 1
Bennett, C. L., Hill, R. S., Hinshaw, G., et al. 2003b, ApJS, 148, 97
Bond, J. R., & Efstathiou, G. 1987, MNRAS, 226, 655
Chiang, L.-Y., & Chen, F.-F. 2011, ApJ, 738, 188
Chiang, L.-Y., & Coles, P. 2000, MNRAS, 311, 809
Chiang, L.-Y., Naselsky, P. D., & Coles, P. 2009, ApJ, 694, 339
Coles, P., & Chiang, L.-Y. 2000, Nature, 406, 376
Doroshkevich, A. G., Naselsky, P. D., Verkhodanov, O. V., et al. 2005, Int. J. Mod. Phys. D, 14, 275
Gold, J., Bennett, C. L., Hill, R. S., et al. 2009, ApJS, 180, 265
Gold, J., Odegard, N., Weiland, J. L., et al. 2011, ApJS, 192, 15
Górski, K. M., Hivon, E., Banday, A. J., et al. 2005, ApJ, 622, 759
Hill, R. S., Weiland, J. L., Odegard, N., et al. 2009, ApJS, 180, 246
Hinshaw, G., Nolta, M. R., Bennett, C. L., et al. 2007, ApJS, 170, 288
Hinshaw, G., Spergel, D. N., Verde, L., et al. 2003, ApJS, 148, 135
Hinshaw, G., Weiland, J. L., Hill, R. S., et al. 2009, ApJS, 180, 225
Hivon, E., Górski, K. M., Netterfield, C. B., et al. 2002, ApJ, 567, 2
Jarosik, N., Bennett, C. L., Dunkley, J., et al. 2011, ApJS, 192, 14
Komatsu, E., Dunkley, J., Nolta, M. R., et al. 2009, ApJS, 180, 330
Komatsu, E., Smith, K. M., Dunkley, J., et al. 2011, ApJS, 192, 18
Larson, D., Dunkley, J., Hinshaw, G., et al. 2011, ApJS, 192, 16
Norta, M. R., Dunkley, J., Hill, R. S., et al. 2009, ApJS, 180, 296
Oh, S. P., Spergel, D. N., & Hinshaw, G. 1999, ApJ, 510, 551
Page, L., Barnes, C., Hinshaw, G., et al. 2003, ApJS, 148, 39
Saha, R., Jain, P., & Souradeep, T. 2006, ApJ, 645, L89
Saha, R., Prunet, S., Jain, P., & Souradeep, T. 2008, Phys. Rev. D, 78, 023003
Samal, P. K., Saha, R., Delabrouille, J., et al. 2010, ApJ, 714, 840
Smoot, G., Bennett, C. L., Kogut, A., et al. 1992, ApJ, 396, L1
Spergel, D. N., Bean, R., Doré, O., et al. 2007, ApJS, 170, 377
Spergel, D. N., Verde, L., Peiris, H. V., et al. 2003, ApJS, 148, 175

[6] http://healpix.jpl.nasa.gov/.
[7] http://www.glesp.nbi.dk/.